Tidal influence on seismic activity during the 2011-2013 El Hierro volcanic unrest

Luis Miguelsanz[1], Pablo J. González[2,3], Kristy F. Tiampo[4], José Fernández[1,*]

[1]Institute of Geosciences (IGEO), CSIC-UCM, Calle del Doctor Severo Ochoa, 7. Facultad de Medicina (Edificio Entrepabellones 7 y 8, 4ª planta), Ciudad Universitaria, 28040-Madrid, Spain.

[2]Volcanology Research Group. Department of Life and Earth Sciences, Instituto de Productos Naturales y Agrobiología (IPNA-CSIC), 38206 La Laguna, Tenerife, Canary Islands, Spain.

[3]COMET. Department of Earth, Ocean and Ecological Sciences, University of Liverpool, Liverpool, L69 3GP, UK.

[4]Cooperative Institute for Research in Environmental Sciences (CIRES), University of Colorado Boulder, USA.

_____

[*]Corresponding author: José Fernández (jft@mat.ucm.es)

Key Points:

- We found significant correlations between tides and volcanic earthquakes during specific phases of the 2011-2013 El Hierro unrest.
- Our results support the hypothesis that tidal stresses may modulate seismicity rates on faults subject to magmatic stressing.
- Tidal modulation sensitivity depends on depth.

Abstract

The El Hierro volcanic unrest started in July 2011, with an increase in observed seismicity rates in and around the island. After the initial onset, hypocenters migrated southward through September 2011 and culminated in a submarine eruption which began on October 10, 2011 and finished in February 2012. However, the seismic activity continued, with remarkable periods of unrest through 2012 and 2013. The most significant episodes of seismic activity during this crisis are related to magma displacements at depth. In this work, tidal stress was calculated at the hypocenter depth for earthquakes from different stages of this crisis, assigning a tidal stress phase angle to each earthquake. We have found statistically significant correlations between the occurrence of earthquakes and certain ranges of tidal stress phase angles in most of the considered scenarios. The analysis of the time period immediately prior to the submarine eruption suggests that tidal compressive stress favored magma displacements towards a shallow magma reservoir. We also found that tidal modulation changes with depth and that the influence of ocean-loading tides is stronger than the influence of solid Earth tides in the correlations. A

41 model based on different scenarios of tidal stress compression or extension is introduced to
42 explain the correlations found in the different stages of seismic unrest. Our results support the
43 hypothesis that tidal stress may trigger earthquakes during volcanic crisis, favoring magma
44 migration, particularly at shallow depths.

45

46

Plain Language Summary

The El Hierro volcanic crisis started in July 2011, with an increase in observed seismicity rates in and around the island which culminated in a submarine eruption that started the 10th of October and finished in February 2012. The seismic activity continued, with remarkable periods of unrest through 2012 and 2013. Tidal values and functions corresponding to the times and locations of the earthquakes were calculated. We have found significant correlations between earthquakes and tides in most of the considered scenarios. The analysis of the time period immediately prior to the submarine eruption suggests that compressive tides favored magma rising towards shallow depths. A conceptual model is introduced to explain the correlations found in the different stages of seismic unrest. Our results support the hypothesis that tides may trigger earthquakes during volcanic crisis, favoring magma migration, particularly at shallow depth.

1 Introduction

Lunar and solar tides rhythmically stress Earth at the tidal periods. These cyclic variations, ranging from 10 to 100 hPa (Tanaka, 2010), appear small compared to earthquake stress drops, which lie between 1000 and 10^5 hPa (Métivier et al., 2009). Nevertheless, tidal stressing is nonlinear in nature and reaches rates of up to 10 hPa/hour, often higher than tectonic stress rates between earthquakes, which reach approximately 0.2 hPa/hour (Emter, 1997). As rapid tidal stresses are superimposed on the far slower, incremental tectonic stresses, they may provide a potential triggering or modulating effect on seismicity rates. As a result, a good deal of research has been carried out that studies the relationship between tides and earthquakes. A detailed review of this subject can be found in the Supporting Information (Text S1).

In this work, we study the correlation between tidal stress and seismicity rates during the volcanic crisis that occurred in El Hierro Island (27.7º N; 18.0º W) between 2011 and 2013. El Hierro is both the youngest and the smallest of the Canary Islands and features the highest concentration of volcanoes in the archipelago (García et al., 2014). The most recent eruption prior to 2011 was in 1793 (Carracedo et al., 2001). The structure of the island is based on three volcanic rifts in directions NE, NW and S (Figure 1a), separated by three important gravitational landslides: El Golfo to the north, Las Playas to the east and El Julan to the south (Masson et al., 2002). Gorbatikov et al. (2013) note the existence of a solidified magma reservoir at the northwest part of the island at a depth between 15 and 25 km. The boundary between the crust and the mantle is set at 12 – 16 km (Watts, 1994; Martí et al., 2017). An intricate array of magma pockets at depths between 12 and 30 km may represent the main magma storage system at El Hierro (Stroncik et al., 2009).

85 The volcanic crisis started in July 2011, with an important increase in seismic activity and
86 ground deformation in El Hierro Island (López et al., 2012; Ibáñez et al., 2012; González et al.,
87 2013). In the first stage, most of the hypocenters concentrated under Tanganasoga volcano and El
88 Golfo valley in the centre and north of the island (Figure 2a). Starting on mid-September, there
89 was a southwards migration of the hypocenters until a submarine eruption occurred offshore of the
90 southern part of the island on October 10-12, 2011 (Figure 2b). After the eruption onset, seismic
91 activity was located in the north around the El Golfo area (Figure 2c). Correlation between gravity
92 variations and tidal vertical strain was observed (Sainz-Maza et al., 2014), suggesting potential
93 tidal triggering of earthquakes during the first days of the eruption. This eruption ended on March
94 5, 2012 (González et al., 2013). However, the seismic activity continued, with periods of high
95 seismicity and deformation through 2012 and 2013 (García et al., 2014) related to magma
96 migration at depth (see Figure 2d-e).

97 Because the rates of diffuse CO_2 emissions may vary before events of volcanic activity
98 (Carapezza et al., 2004), estimating the output of this gas has implications in early warning systems
99 applied to volcanoes. In the case of El Hierro Island, diffuse CO_2 emission have been monitored
100 since 1998 (Melián et al., 2014), and especially during the seismo-volcanic crisis that started in
101 July 2011. Through the analysis of these measurements of CO_2 emission, Melián et al. (2014)
102 found two remarkable periods of efflux increase that may be considered as precursory signals. The
103 first one occurred between 29 September and 12 October, i.e., starting almost two weeks prior the
104 beginning of the submarine eruption and ten days before an event of magnitude M = 4.3. The
105 second significant increase in the rate of diffuse CO_2 emission occurred during the period 24
106 October to 27 November, preceding both the bubbling observed at the sea between 3 and 7
107 November and the M = 4.6 event recorded on November 11. However, the time series of diffuse

CO_2 emission in El Hierro Island does not show any correlation to meteorological parameters such as rain, soil moisture or barometric pressure (see Figure 7 by Melián et al. (2014)).

2 Seismic and volcanic activity related to El Hierro (2011-2013)

Following the analysis of the seismicity by Ibáñez et al. (2012), we can identify different phases in the seismic activity of El Hierro during the period 2011 to 2013, which are related to different spatial settings of the earthquakes or different stages in the magma migration processes.

In this work, we designate all seismicity prior to the eruption occurred on October 10, 2011, as *Phase 1*. This episode starts with an abnormal increase of earthquakes in July 17, 2011 (Figure 2a). During this period, magma is detected as an intrusion in the base of the oceanic crust (around 9.5 km depth), at the south of the main concentrations of earthquakes (González et al., 2013).

Around mid-September 2011, epicenters start migrating to the south of the El Golfo area (Figure 2b). GPS stations detect north-south deformation, suggesting that magma was migrating away from the magma intrusion site (crust-mantle reservoir, CMR (González et al., 2013). Hypocenters are (on average) deeper than before, and average earthquake magnitudes also are greater (Ibáñez et al., 2012). At the end of September, magma began an upward migration, accumulating at a shallower magma reservoir at around 4.5 km depth. This reservoir likely failed around October 8 with an event of magnitude $M = 4.3$ that opened a path for magma towards the surface (Figure 1b). Later, between October 10 and 12, the submarine eruption began (González et al., 2013).

On 15 October 2011, new seismic activity was located in the north around the El Golfo area. We will consider this a separate stage (*Phase 2*; Figure 2c) in the seismic activity, as these

earthquakes happen far from the eruption site, in the opposite side of the island. Hypocenters in *Phase 2* are deeper than in *Phase 1*, with a depth range between 15 and 25 km (Ibáñez et al., 2012). Four of the earthquakes that occurred during *Phase 2* show magnitudes $M > 4$, including an $M = 4.6$ event recorded on November 11, 2011. The seismic activity decreases progressively through December 2011, although there are some earthquakes during January and February 2012, as well as some visible effects of the submarine eruption on the sea surface. The end of the eruption was officially decreed in March 5, 2012. See González et al. (2013) for a detailed description on the seismic and volcanic activity during *Phases 1* and *2*.

After the ending of the submarine eruption, new episodes of seismic activity occurred, the most relevant (in terms of number of earthquakes) being those recorded primarily in June-July 2012 and March-April 2013. For the purposes of this research, we will refer to these two crises as *Phase 3* (2012-06-14 to 2012-08-21; Figure 2d) and *Phase 4* (2013-03-17 to 2013-04-30; Figure 2e). Some authors think that there is oceanographic and geochemical evidence that the seismic activity in *Phase 3* is coincident in time with submarine volcanic activity offshore the western coast of El Hierro (Pérez et al., 2014; García-Yeguas et al., 2014), but this volcanic activity must be interpreted in terms of magma injection processes that do not necessarily culminate in an eruptive process (Blanco et al., 2015; Pérez et al., 2015). There is no evidence of new eruptions near El Hierro island after the one that occurred between October, 2011 and March, 2012, although several authors do suggest that the magmatic processes around El Hierro island continued after the conclusion of that eruption (García et al., 2014). Hypocenters in *Phase 3* are located under the west wing of the island, whereas events in *Phase 4* are, on average, the most distant from the island. It is during *Phase 4* that the strongest seismic activity took place, in

addition to the largest magnitude earthquake (M = 4.9) and the greatest number of landslides (García et al., 2014).

3 Study of the seismicity and Earth tides correlation

3.1 Earthquake data

Seismicity data related to the El Hierro volcanic crisis were obtained from the Spanish Geographical Survey, IGN [www.ign.es]. Our main data source is a catalog featuring all earthquakes within the period 17/07/2011 – 31/12/2013, and including event number, date, time, latitude, longitude, depth, intensity, magnitude, magnitude type and location area. Very low magnitudes are excluded because the location of small earthquakes may be affected by significant errors, especially in a small island like El Hierro (García et al., 2014). Therefore, we used only earthquakes with magnitude $M_c \geq 1.5$, where M_c is the minimum magnitude of completeness based on a frequency-magnitude distribution analysis using the Maximum Curvature (MAXC) technique (Mignan and Woessner, 2012). In addition, in the case of the earthquakes that occurred during *Phase 1*, we used the catalog of Domínguez Cerdeña et al. (2014), where all events previous to the submarine eruption with magnitude $M \geq 1.5$ were relocated using program hypoDD (Waldhauser and Ellsworth, 2000), which improved the precision in the location of earthquakes by as much as 10 times. This relocated catalog also is accessible from the IGN website. The best-fitting double-couple fault plane solution for a set of observed first motion polarities is provided only for one event, so fault mechanisms will not be considered in this study.

Application of the declustering algorithm of Reasenberg (1985) to the catalog shows that for each one of the four phases there exists one big cluster which includes 90 – 95 % of the

178 events that occurred during that phase. The list of parameters used in the declustering process
179 (van Stiphout et al., 2012) can be found in the Supporting Information (Table S1). Figure 3
180 shows the location of the earthquakes in each *cluster C1 – C4*. A visual comparison between
181 Figure 2 and Figure 3 suggests that, in every *Phase i* (i = 2,3,4), most of the events not belonging
182 to the corresponding *cluster Ci* may be a remnant or continuation of previous phases, implying
183 that they are not necessarily related to the magma movements or physical processes which
184 originated each phase. As a result, only the events in the *clusters C1 – C4* have been considered
185 here, as we are going to study the possible modulation effects of tides on seismicity in each one
186 of the four phases independently.
187 Tidal stress and strain were calculated for the locations of all events in each cluster, in
188 order to estimate statistical correlations for tidal modulation of the occurrence of earthquakes in
189 the different phases of the seismic crisis.

190

191 3.2 Calculation of tides

192

193 In order to obtain the tidal stress at the earthquake locations, it is necessary to consider
194 both the solid tide and the ocean tide. In addition, the calculation must include the depth of the
195 events. Strains derived from the solid tides at depths less than 25 km are not significantly
196 different from surface strains but strains due to the ocean loading component may change
197 significantly between the surface and a depth of 25 km (Thomas et al., 2012).
198 Our method uses the software package SPOTL (Agnew, 2012) for the calculation of tidal
199 strains. Body tides are calculated on an elastic Earth following Munk and Cartwright (1966). The
200 ocean tidal model we have used is osu.tpxo72atlas (Agnew, 2012), which is a hydrodynamic

model assimilating altimetry data from TOPEX/Poseidon and Jason. It combines three basin-wide solutions (Atlantic Ocean 2011-atlas, Pacific Ocean 2011-atlas and Indian Ocean 2011-atlas), each one of which also incorporates a set of high-resolution local models. Tidal waves considered in the study are M_m, M_f, Q_1, O_1, P_1, K_1, N_2, M_2, S_2, K_2. The original SPOTL codes where modified to use depth-dependent Green functions in the calculations, following the methodology described in Royer et al. (2015) for the modeling of tidal strains at depth. Then tidal stresses are derived from tidal strains following Hooke's law for a tridimensional isotropic body (Fischer et al., 2006), with Poisson's ratio $\nu = 0.25$ and rigidity $\mu = 30$ GPa. We consider positive stress as extension.

To study the correlations between tides and earthquakes, we assign a phase angle, ϕ, to each event, which can be evaluated later in statistical terms. For this purpose, a golden section search routine (Press et al., 1992) is used to estimate the extreme tidal values closest to the time of occurrence of the event. Finally, we assign the phase angle ϕ to the earthquake by linear interpolation, assuming the time distance between two tidal peaks defines a complete cycle of 360º (see Figure 4).

3.3 Statistical methods

The Schuster test was used in order to determine whether there is a non-random distribution of the calculated tidal phases (Emter, 1997). In this test, each *i*-th earthquake is assigned a unit length vector in the direction of the phase angle ϕ_i. The modulus R of the vector sum **R** over the total number of earthquakes N_{tot} is given by

$$R^2 = \left(\sum_{1}^{N_{tot}} \cos \phi_i \right)^2 + \left(\sum_{1}^{N_{tot}} C \sin \phi_i \right)^2 \quad (1)$$

where C is a factor correcting local asymmetries in tides (Wilcock, 2009). It must be noted that no significant tidal asymmetries where found in El Hierro in the time periods considered in this study, as all C values observed for tidal strain or tidal stress are in the range 1 ± 0.0020.

Then, the probability P_s that the phase distribution to be non-random is estimated by

$$P_s = \exp\left(\frac{-R^2}{N_{tot}} \right). \quad (2)$$

P_s represents the significance level with which to reject the null hypothesis that the earthquake phase angles represent a completely random distribution. Small values of P_s (< 0.05) indicate the existence of a high correlation between tidal stress and the occurrence of earthquakes.

As we are treating highly clustered seismicity, we are not dealing with independent earthquakes. Given the high sensitivity of the Schuster test (Emter, 1977), that means the catalog may be biased in a way that favors the rejection of the null hypothesis. One way to assess the significance of the observed P_s values is the use of a Monte Carlo permutation test (Noreen, 1989; Fortin and Jacquez, 2000). For each of the four *clusters C1 – C4* we order the earthquakes according to their phase angle ϕ, and we divide them into segments (phase angle ranges) of equal length (different segment lengths are tested, see next section). Then, a number *NSIM* of simulations (e.g., 10000 simulations) are performed for each cluster with the segments in random

order, obtaining a probability value P_s* according to the Schuster test for each simulation. Finally, for each cluster we count the number *NSIG* of random simulations in which the P_s* value obtained is lower than the P_s value of the original distribution of events. The ratio

$$MC_{sl} = \frac{(NSIG + 1)}{(NSIM + 1)} \quad (3)$$

provides the significance level of our test (Noreen, 1989).

In addition, the American Statistical Association (ASA) expresses concern regarding the hypothesis testing based on *p*-values, stating that these practices are prone to generate false positives (Wasserstein and Lazar, 2016). Bayarri et al. (2016) propose a simple alternative to the use of *p*-values in testing null hypothesis, based on the Bayes factor *B*, which is defined as

$$B = \frac{average\ likelihoo\quad of\ the\ observed\ data\ under\ the\ alternative\ hypothesis}{likelihoo\quad of\ the\ observed\ data\ under\ the\ null\ hypothesis} \quad (4)$$

Although *B* may be difficult to compute, it can be approximated by an upper bound $\overline{B}$ which is a function of the *p*-values obtained with the usual statistical tests used in testing hypothesis. According to Bayarri et al. (2016), and considering the Schuster test as the appropriate one for our null hypothesis testing:

$$B \leq \overline{B} = \frac{1}{-eP_s \log P_s} \quad (5)$$

Here we use the *p*-values P_s calculated by means of the Schuster test to derive this upper bound $\overline{B}$ of the Bayes factor *B*. According to Bayarri et al. (2016), the standard significant threshold for rejecting the null hypothesis when using this Bayesian alternative is $\overline{B} > 16$.

The use of this Bayesian method is a new application to the assessment of correlations between tides and earthquakes, and it has implications for earlier studies of tidal triggering of seismicity where the statistical significance was primarily based on *p*-values.

4 Results

Results for the application of the Schuster test to the earthquake clusters defined in section 3.1 are shown in Table 1. The upper bound $\overline{B}$ of the Bayes factor *B* is also shown in Table 1 in order to compare results. According to the Schuster test, very high correlation ($P_s < 0.05$) appears in three of the four *clusters* (*C1*, *C3* and *C4*) between tidal confining stress (i.e., the trace of the tidal stress tensor) and the occurrence time of earthquakes. However, when we consider the value of the upper bound of the Bayes factor, only the correlations for *clusters C1* and *C4* are statistically significant.

Table 2 shows the results of a Monte Carlo permutation test (10000 simulations) applied to the earthquake *clusters C1-C4*, following the methodology explained in section 3.3. For each *cluster*, the corresponding catalog has been divided into 72 segments of 5º width. Different segment sizes may produce different results, because the greater the segment length is, more patterns from the original distributions are repeated in the simulations and the number of possible permutations diminishes (Bhatnagar et al., 2016). As a result, a catalog divided into 144 segments of 2.5º width was also tested (see Table 2). According to this permutation test, the

289 correlation is statistically significant for *clusters C1*, *C3* and *C4*, although the value of the
290 significance level, MC_{sl}, provided for cluster *C3*, is clearly higher (implying a weaker statistical
291 significance) than those obtained for *clusters C1* and *C4*. On the other hand, the random
292 shuffling of segments in *cluster C2* distribution produces a great number of P_s* values lower
293 than the original P_s value for both segment lengths considered here, meaning that the correlation
294 is not statistically significant.

295 Figure 5 shows the histograms of the frequency distributions of tidal confining stress phase
296 angles for *clusters C1*, *C2*, *C3* and *C4*, respectively. In these histograms, earthquakes are
297 collected in phase angle ranges of 30º width. The sinusoidal curve applied to the frequency
298 distributions is obtained by least squares fitting of the expression

299

300 $$P(\phi) = P_0 + P_1 \cos(\phi - \alpha), \qquad (6)$$

301

302 where ϕ is the phase angle, P_0 is the mean frequency, P_1 is the amplitude of the curve and α is
303 the phase of the curve (Tanaka et al., 2002). A triangle marks the peak of the fitted curve
304 associated to the histogram, which occurs on the phase angle maximizing eq. (6).

305 Figure 5a shows that the histogram corresponding to *cluster C1* (coincident with *Phase 1*
306 in the seismic crisis, i.e., all the seismicity prior to the starting of seismic tremor signal) is clearly
307 biased towards the right side of the phase angle axis, the phase range where tidal stress is
308 increasing ($180º < \phi \leq 360º$). The fitted curve peaks around phase angle $\phi = 251º$. As seen in
309 Tables 1 and 2, the correlation between confining tidal stress and the occurrence of earthquakes
310 in *cluster C1* is remarkably high for every statistical test. The histogram corresponding to *cluster*
311 *C2* (Figure 5b) does not show a statistically significant correlation with any of the applied

312 methods, although the most populated phase angle range is $270^o < \phi \leq 300^o$. *Cluster C3*
313 corresponds to *Phase 3*, the seismic activity recorded during June-August 2012 under the
314 northwest rift. According to the Schuster test and the Monte Carlo permutation test, there also is
315 high correlation between tidal stress and the occurrence of earthquakes, although both the P_s
316 statistical and the ratio MC_{sl} are not as conclusive as those obtained for *cluster C1*. Besides, the
317 correlation is not significant if we consider the application of the upper bound $\overline{B}$ of the Bayes
318 factor B (Table 1). The fitted curve for *cluster C3* distribution has a peak around $\phi = 209^o$ (Figure
319 5c). Finally, the histogram obtained from *cluster C4* data (Phase 4, which includes the seismicity
320 observed during 2013 March-April and expanding offshore eastwards) is similar to the *cluster*
321 *C1* histogram, with a distribution biased towards the phase angle range where confining tidal
322 stress is increasing ($180^o < \phi \leq 360^o$), and a fitted curve whose peak lays around $\phi = 288^o$ (Figure
323 5d). All the statistical tests considered for *cluster C4* data suggest very high correlation (Tables 1
324 and 2).

325 As some of the distributions (namely the histograms corresponding to *clusters C1* and *C4*)
326 show an apparent bias towards phase range $180^o < \phi \leq 360^o$, a simple binomial test (see e.g.,
327 Wonnacot and Wonnacot, 1977) was performed in order to evaluate if the events are more prone
328 to happen in the increasing-tide half cycle ($180^o < \phi \leq 360^o$) rather than in the decreasing-tide
329 half cycle ($0^o < \phi \leq 180^o$). The results of applying that test to the four clusters appear in Table 3,
330 showing very high correlation in the cases of *clusters C1* and *C4*, and a poor correlation (not
331 statistically significant) for *clusters C2* and *C3*. The upper bound $\overline{B}$ of the Bayes factor B has
332 also been calculated for the probability value P_i derived from the binomial test (Table 3).
333

5 Discussion

The initial results from the statistical tests (Tables 1, 2, and 3) and the analysis of the phase angle distribution (Figure 5) suggest that the earthquakes belonging to *clusters C1* and *C4* are highly correlated with tidal confining stress, supporting the hypothesis that tidal stress may trigger earthquakes, especially in the case of events related to volcanic areas (Rydelek et al., 1988; Emter, 1997), and therefore facilitate the magma migration process. The absence of correlation in the case of *cluster C2* may be due to the fact that most of the seismicity belonging to that period of time (2011-10-17 to 2012-01-01) may be related to the collapse of deep sections of the magma plumbing system as magma withdrew (Martí et al., 2013; González et al., 2013), instead of produced by a progressive magma migration process (González et al., 2013) as in *Phase 1* (*cluster C1*), or the post-eruption *Phase 4* (*cluster C4*), which was also associated with migration of magma (García et al., 2014).

Finally, the correlation between earthquakes and tidal confining stress in the events belonging to *cluster C3* is doubtful. The probability values corresponding to the Schuster test and the Monte Carlo permutations test are statistically significant based on the commonly-used 0.05 threshold, even though they are higher (implying a weaker correlation) than the values obtained for *clusters C1* or *C4*. But if we consider the value of the upper bound $\overline{B}$ of the Bayes factor B (Table 1), where the threshold for statistical significance is $\overline{B} > 16$, the result is no longer significant. Nevertheless, the earthquakes in *cluster C3* occurred during the post-eruption process we are calling *Phase 3*, where magma migration also occurred (García et al., 2014), so a weak correlation should not be ruled out.

It should be noted that there are differences in the frequency distributions obtained for the different *clusters* (Figure 5). The peak of the sinusoidal curve lies around tidal stress phase angle

358 ϕ = 288º (i.e., close to the maximum tidal stress) in the histogram related to *cluster C4* (Figure
359 5d). For the *cluster C1* histogram it is centered at ϕ = 251º (i.e., halfway between minimum tidal
360 stress and maximum tidal stress; Figure 5a), while the histogram for *cluster C3* is around ϕ =
361 209º, close to the minimum tidal stress, although still in the increasing leg of the tidal stress
362 frequency distribution (Figure 5c). These differences may be due to the different types of focal
363 mechanisms controlling the seismicity in the clusters and/or also related to the depth of the
364 earthquakes, as controlled by magma location.

365 As suggested elsewhere (Tanaka, 2002; Xu et al., 2011), the trend of the correlation
366 between tidal stress and the occurrence time of earthquakes may vary according to the type of
367 fault. Due to the lack of information about focal mechanisms in the earthquake catalog used, an
368 analysis of tidal stress triggering according to faulting type in the El Hierro volcanic crisis is
369 beyond the scope of this work, but it should be considered in the future, if additional information
370 becomes available.

371 Figure 6 provides additional information about tides and seismicity in the context of the
372 submarine eruption occurred at the end of *Phase 1*. We have calculated tidal volume strain in the
373 setting of the shallow reservoir (latitude 27.6653º, longitude -18.0370º, depth 4.5 km; see
374 González et al., 2013) at two-hour intervals during the time period covered by *Phase 1*, and we
375 have compared it to the number of earthquakes in *cluster C1* recorded every two hours during the
376 same time period.

377 The plot is divided in two parts, with the beginning of the southward migration of
378 earthquakes on September 15, 2011, marking the separation between the two. During the first
379 period (Figure 6a; 2011-07-15 to 2011-09-14) no clear correlation appears between the biggest
380 earthquake swarms recorded and the highest (or lowest) tidal amplitudes in the fortnightly

period. In fact, most of the swarms seem to occur when the upper envelope of the tidal strain amplitudes graph is low (or the lower envelope is high), which seems counter-intuitive. On the other hand, in the second period (Figure 6b; 2011-09-15 to 2011-10-15) it is obvious that the most significant episodes of seismic activity prior to the submarine eruption of October 10, 2011 began around September 26, 2011, when the tidal volume strain graph is close to its extreme values. This also is the time when magma begins the upward migration towards the shallower magma reservoir, as shown by González et al., (2013), which suggests that tidal strain can trigger earthquakes favoring magma migration at shallow depths. Similar figures covering *Phase 2*, *Phase 3* and *Phase 4* are provided as Supporting Information (Figures S1 – S3).

In order to investigate tidal triggering in the period immediately prior to the submarine eruption, we divided the *cluster C1* in two *sub-clusters*: *C1A* (2011-07-21 to 2011-09-25) and *C1B* (2011-09-26 to 2011-10-10, starting with the upward movements of magma to the shallower reservoir). The results of the application of the statistical tests to *sub-clusters C1A* and *C1B* are summarized in Table 4, whereas the histograms of the frequency distributions of confining tidal stress phase angles are shown in Figure 7.

As in *cluster C1*, both *sub-clusters C1A* and *C1B* show high correlation between confining tidal stress and the occurrence time of earthquakes (Table 4), but there is a significant difference between both distributions. The peak of the fitted curve lies around tidal stress phase angle $\phi =$ 279º (which is halfway between minimum tidal stress and maximum tidal stress, although closer to the maximum) in the histogram related to *sub-cluster C1A* (Figure 7a). For the *sub-cluster C1B* histogram, it lies around $\phi =$ 216º (i.e., close to the minimum tidal stress), with a large number of events concentrating on the tidal phase range $150º < \phi \leq 210º$, central to the distribution (Figure 7b). As we consider tidal stress positive in extension, minimum tidal stress is

indeed maximum tidal stress in compression. This suggests that, during the period of upward migration of magma towards the shallower magma reservoir, tidal compressive stress favors these magma displacements and the subsequent seismic activity. Figure S4 in Supporting Information features a study of tidal confining stress amplitudes corresponding to the earthquakes in *sub-clusters C1A* and *C1B* which supports this interpretation.

These results suggest that there are different tidal modulations of the seismic events related to magma ascent, depending on the depth. In order to continue testing the sensitivity of the correlation to depth, we have focused on tidal confining stress, and we have considered 15 km depth as a threshold, as the boundary between the crust and the mantle lies at 15-16 km in the vicinity of the Canary Islands (Watts, 1994). In *sub-clusters C1A* and *C1B*, where most of the events belong to the depth range 10 – 15 km, high correlation is found between confining tidal stress and the occurrence time of earthquakes (see Table 4). In *cluster C2*, where the vast majority of events are > 15 km depth, there is no statistically significant correlation with tides, as seen in Tables 1 and 2. In *cluster C3*, where, again, the great majority of hypocenters are in depth values > 15 km, the correlation is clearly lower than in *sub-cluster C1A* or *sub-cluster C1B* (see Tables 1 and 2). Finally, in *cluster C4* we have considered two *sub-cluster*: *C4A* (earthquakes with hypocenters in the depth range between 0 and 15 km, 526 events), and *C4B* (earthquakes with depth > 15 km, 1556 events). Table 5 shows the results of the application of the statistical tests defined in section 3.3 to both *sub-clusters C4A* and *C4B*. In all cases, *sub-cluster C4A* gives a high correlation with tidal confining stress that is better than the one obtained for the whole *cluster C4* (as seen in Tables 1 and 2). Figure 7c shows the histogram of the frequency distribution of tidal confining stress phase angles for *sub-cluster C4A*. The most populated tidal phase range is $240^{\circ} < \phi \leq 270^{\circ}$, and the peak of the fitted curve lies around tidal stress phase

angle $\phi = 300^{o}$, a value quite close to the maximum of the fitted curve corresponding to the entire *cluster C4* (Figure 5d). On the other hand, there is no statistically significant correlation with tidal confining stress for *sub-cluster C4B* (Table 5). These results suggest that tidal stress correlation with the origin times of the earthquakes is better for events whose hypocenters are at crustal levels.

So far, our results suggest that there is a correlation between tidal stress values and the occurrence of earthquakes during the 2011 – 2013 volcanic crisis in El Hierro island. But stressing-rate could be the controlling factor, rather than maximum/minimum values. That being the case, the strongest gradients of tidal variations might be more important for triggering of earthquakes than the absolute value of the tidal stress, as it was noted by McNutt and Beavan (1981) and McNutt and Beavan (1984). With that in mind, we calculate tidal confining stress rates corresponding to all earthquake *clusters* or *sub-clusters C1A*, *C1B*, *C2*, *C3*, *C4A* and *C4B*, and attempt to determine if the events occur more frequently when tidal stress rate is higher. The corresponding histograms appear in Figure 8, and the results for the statistical tests are shown in Table 6. There are three *clusters* with statistically significant values for all the tests defined in Section 3.3, namely *C1A* (Figure 8a), *C1B* (Figure 8b) and *C4A* (Figure 8e). There are no significant correlations between earthquakes and tidal stress rates in the events belonging to *clusters C2* (Figure 8c) and *C4B* (Figure 8f). Finally, the correlation for *cluster C3* appears to be statistically significant when using the Schuster test or the Monte Carlo permutations test, but it is not significant when considering the upper bound $\overline{B}$ of the Bayes factor B (Table 6), so this correlation must be considered with caution. In addition, in most of these *clusters* (Figures 8a, 8c, 8d, 8e, 8f), the most frequently occurring phase angle range is the high-tide half cycle ($0^{o} \leq \phi < 90^{o}$ or $270^{o} \leq \phi < 360^{o}$), where tidal confining stress rates are higher. The exception here is

450 *sub-cluster C1B* (Figure 8b), where the highest frequency corresponds to phase angle range 240º
451 $\leq \phi <$ 270º. It should be noted that, in the time period covered by *sub-cluster C1B*, our previous
452 analysis of tidal strain and stress values suggests that tidal compression plays a key role in
453 earthquake triggering, rather than tidal extension, and this could explain the difference in
454 behavior of *sub-cluster C1B*.

455 Our analysis of tidal triggering of earthquakes in El Hierro based on tidal stress rate
456 agrees with the results from our previous analysis based on tidal stress values (Tables 1, 2, 4 and
457 5), in the sense that the subsets of events where the statistical significance is poorer are *clusters*
458 *C2*, *C3* and *sub-cluster C4B*, which are mostly composed of earthquakes > 15 km depth, even
459 though in the case of *cluster C3* the results are still statistically significant for both Schuster and
460 Monte Carlo tests. If we discard *clusters C2* and *sub-cluster C4B* (as they obtain the worst results
461 with all the statistical tests considered), there is an interesting similarity between the frequency
462 distributions of *clusters C1A* and *C4A*, and between *cluster C3* and *sub-cluster C1B*. Whereas the
463 maximum of the fitted curve in the distributions of *sub-clusters C1A* (Figure 8a) and *C4A*
464 (Figure 8e) lies around extreme values of the tidal stress rate cycle ($\phi =$ 356º and $\phi =$ 11º,
465 respectively), it is centered close to $\phi =$ 290º in both frequency distributions for *sub-cluster C1B*
466 (Figure 8b) and *cluster C3* (Figure 8d). Although the correlation found for *cluster C3* is not as
467 consistent as the one obtained for *sub-cluster C1B* (it is not statistically significant when we
468 apply the Bayesian alternative to p-values) these results may reflect that, in the case of *cluster C3*
469 and *sub-cluster C1B*, tidal compression plays an influence in promoting magma movements
470 towards shallow depths. Finally, we have seen that both seismic activities belonging to *sub-*
471 *cluster C1B* and *cluster C3* can be related to volcanic activity due to magma injection processes,
472 even though these processes only ended with an eruption in the case of the *cluster C1B* activity.

In all the time periods considered in this study, ocean-loading tides are stronger than solid Earth tides. According to Cochran et al. (2004), tidal stresses due to body tides can reach values up to 5 x 10^3 Pa, which is one order of magnitude less than the values that can be reached by tidal stresses induced by ocean loading tides (5 x 10^4 Pa) in ocean basins. For all the events in the different clusters in the study, we have calculated half cycle amplitudes (see definition in Figure 4) induced by ocean tidal loading confining stress and half cycle amplitudes due to Earth tidal confining stress. The former is, on average, between five and six times greater than the latter, depending on the cluster (see data in the repository https://zenodo.org/record/3714198#.YDX_OXlPGUl). Therefore, the ocean tidal signal appears to be more important than the body tidal signal in the modulation of the seismic activity during the El Hierro volcanic crisis. This result could be of general application in many of the volcanic events in oceanic islands and should be confirmed with additional, complementary studies.

In order to show if the magnitude cutoff chosen for the catalogs is relevant in the results obtained, we have performed some of the statistical tests over the catalogs removing all earthquakes with $M < 2$. As seen in Table S2 in the Supporting Information, the results are quite similar to the ones obtained in the original analysis, where $M = 1.5$ was the lower magnitude cutoff. We have not performed the statistical tests over declustered catalogs because, as we have told in Section 3, this seismicity is highly clustered in such a way that replacing each cluster for the biggest or the first event in the cluster series results in catalogs with very few elements. An example is shown in Table S3 in the Supporting Information, where a declustering process using a cutoff of $M = 2.5$ is described. Table S4 in the Supporting Information provides a more detailed description of the declustered catalogs D1-D4 so produced.

We have tested also possible correlations between earthquakes and strong rains in the island. Meteorological data are provided by the Spanish Meteorological Agency (AEMET) (http://www.aemet.es/es/datos_abiertos). Figures S5, S6 and S7 in the Supporting Information show the comparative between earthquakes and pluviometry during the periods covered by *clusters C1*, *C2* and *C4* (there is no graph for *cluster C3* because apparently there was no rain during that time period). Although some correlation seems to exist between rains and some parts of the earthquakes sequences (mainly for *cluster C4*, see Figure S7), it must be noted that the only data source for the rains is Hierro Aeropuerto Station, which is located at the northeast of the island and whose data may not be usable for all the locations of the earthquakes.

Our interpretation of the volcano dynamics that generate the various tidal correlations found in this work is detailed in Figure 9. During the time period 2011-07-17 to 2011-09-25 (*sub-cluster C1A*), magma begins to accumulate in the deep CMR, and then migrates longitudinally around the center of the CMR (Figure 9a). In this context, at low tide and the lowering of sea level, the weight of the ocean over the seafloor around the island diminishes, resulting in a decrease in compression and an increase in extension. High values of extensional tidal confining stress rates may favor magma displacement and encourage extensional faulting. The seismic activity related to this time period may be biased to higher values of tidal stress rates. On the other hand, during the period defined by *sub-cluster C1B* (2011-09-26 to 2011-10-10), magma ascends towards the shallower reservoir, which is smaller than the CMR, and accumulates there until the eruption started on October 10, 2011 (Figure 9b). As the longitudinal displacement is almost nonexistent, magmatic activity in the shallow reservoir may be more sensitive to small changes in tidal stress compression. At high tide, sea level rises and the compression exerted on the seafloor by the body of water increases, promoting magma ascent

and the build-up of pressure within the magma chamber. Tidal confining stress compression, together with tectonic and volcanic stresses, would encourage magma to migrate into zones of weakness to ascend, favoring seismic activity in the process. Note that Figure 7b suggests that it is tidal compressive stress which promotes the seismic activity related to this period.

There appears to be no correlation between tides and seismicity during the co-eruption phase, to which the earthquakes in *cluster C2* belong (2011-10-17 to 2012-01-01). As suggested before, one possible reason is that seismicity could have originated with the collapse of deep sections of the magma plumbing system as magma withdrew (Martí et al., 2013; González et al., 2013), rather than being produced by a progressive magma migration process (González et al., 2013). For the correlation between tidal confining stress and earthquakes in *cluster C3*, a mechanism based on tidal compression similar to that described in Figure 9b is a possible explanation, as we know that the earthquakes belonging to that period can be related to volcanic activity due to magma injection processes under the west wing of the island (Blanco et al., 2015). Nevertheless, more research is needed in order to confirm that this correlation is a function of the proposed physical mechanism because the hypocenters in *cluster C3* are at deeper depths than those ones of *sub-clusters C1A* or *C1B*. In addition, the correlation found in *cluster C3* is poorer than those obtained for *sub-clusters C1A* or *C1B*, and it is not statistically significant when we estimate the upper bound of the Bayes factor (Tables 1 and 6).

Finally, a look at the dispersion of the hypocenters of the events in *cluster C4* (see Figure 3d) suggests important magma displacements in longitude. In this context, the mechanism described in Figure 9a, based on extensional tidal confining stress rates promoting magma displacements and related seismic activity, may provide an explanation to the correlations found for *cluster C4* and the *sub-cluster C4A*. The lack of correlation in the case of *sub-cluster C4B*

(even though its hypocenter distribution is similar to the original *cluster C4*, as seen in Figure S8 in the Supporting Information) may be due to the greater depth of the events when compared to those in *sub-cluster C4A*.

6 Conclusions

In July 2011 a volcanic crisis started in El Hierro Island with an increase in observed seismicity rates in the island, with remarkable periods of unrest through 2012 and 2013, even after the submarine eruption that occurred between October 2011 and February 2012. During the period studied here, hypocenters were migrating spatially. We have studied the correlation within the seismicity and the tidal stress calculated at hypocenter depth for the earthquakes of different stages of this crisis, assigning a tidal stress phase angle to each earthquake. Our results show correlation between tidal stress and the origin times of the earthquakes in the context of volcanic areas, with tides enhancing magma movements at depth, confirming that tidal stress can play a role in the triggering of an eruption if the magma system is in a critical state at shallow depths (Sottili et al., 2007).

Although correlation between residual gravity and body tide vertical strain was found by Sainz-Maza et al. (2014) during the first three days of the eruption, suggesting concurrent tidal triggering during the beginning of the eruption, the work presented here is the first study of the recent volcanic crisis in El Hierro focused on the influence of tides in the seismic activity and covering the most significant phases of the 2011-2013 El Hierro unrest.

Summarizing, we have found that tidal stress values and tidal stress rates are correlated with the occurrence times of the earthquakes in different phases during the volcanic crisis at El

Hierro. In addition, the analysis of the time period immediately prior to the submarine eruption suggests that tidal compressive stress favored magma displacements towards the shallower magma reservoir. Tidal modulation also seems to be dependent on depth. We also determined that the influence of ocean-loading tides is stronger than the influence of solid Earth tides in the correlations presented here. We present a conceptual model (see Figure 9) to explain the different correlations between tides and earthquakes found in the different phases in terms of the influence of tidal compression or tidal extension in the magma movements at depth.

Our results, using tidal strains and stresses calculated for thousands of earthquakes at hypocenter depth, applying depth-dependent Green functions and the most recent ocean models available, agree with some previous studies (e.g., Dzurisin, 1980; Rydelek et al., 1988; Berrino and Corrado, 1991; Kasahara et al., 2001; or Bhatnagar et al., 2016). Some of them also show a different polarity according to compression or extension stress or strain (McNutt and Beavan 1981; 1984; Scholz et al., 2019). Our conclusions support the hypothesis that tides may produce a modulation of the earthquake activity in volcanic areas, in particular when magma arrives to shallow depths.

These results, obtained for the volcanic crisis where the last eruption in Canary Islands took place, should be considered in the study of future volcanic reactivation in the archipelago and other volcanic islands. Implications for volcano hazard monitoring may be important, as seismic monitoring of active volcanoes is one of the primary methods for characterizing activity levels and is a significant factor in assessing associated hazard probabilities. Insights into the impact of tidal forces on the seismic activity on active volcanoes have the potential to improve our understanding of volcano dynamics and better quantify eruption hazard.

Acknowledgments, Samples, and Data

This research was mainly funded by the Spanish Ministerio de Ciencia, Innovación y Universidades research projects DEEP-MAPS, grant agreement number RTI2018-093874-B-I00, and COMPACT, grant agreement number PID2019-104571RA-I00, and also partially by MINECO research project ESP2013-47780-C2-1-R and CSIC project 201530E019. P. J. González research was partially supported by the UK NERC through the NE/K011006/1 and COMET (GA/13/M/031, http://comet.nerc.ac.uk) projects, and the Beca Leonardo a Investigadores y Creadores Culturales 2020 of the Fundación BBVA. The work also was supported by CIRES, University of Colorado Boulder. We thank the comments by M. Lupi and one anonymous reviewer which help us to improve a previous version of this manuscript. We thank Amanda Thomas for providing the depth-dependent Green functions. This is a contribution of the CSIC Thematic Platform Volcanism and Society (www.ptivolcan.es). Used seismic catalog can be downloaded from IGN website, www.ign.es. The remainder of the data is available in the repository https://zenodo.org/record/3714198#.YDX_OXlPGUl

References

Agnew, D.C. (2012). SPOTL: Some Programs for Ocean-Tide Loading. *SIO Technical Report, Scripps Institution of Oceanography*. http://escholarship.org/uc/item/954322pg.

Berrino, G., & Corrado, G. (1991). Tidal signal in the recent dynamics of Campi Flegrei caldera (Italy). *Journal of Volcanology and Geothermal Research, 48*, 93-101.

608 Bhatnagar, T., Tolstoy, M., & Waldhauser, F. (2016). Influence of fortnightly tides on
609 earthquake triggering at the East Pacific Rise at 9°50'N. *Journal of Geophysical Research*
610 *Solid Earth, 121*, 1262–1279. doi:10.1002/2015JB012388.
611 Blanco, M.J., Fraile-Nuez, E., Felpeto, A., Santana-Casiano, J. M., Abella, R., Fernández-Salas,
612 L. M., Almendros, J., Díaz-del-Río, V., Domínguez Cerdeña, I., García-Cañada, L.,
613 González-Dávila, M., López, C., López-González, N., Meletlidis, S., & Vázquez, J. T. (2015).
614 Comment on "Evidence from acoustic imaging for submarine volcanic activity in 2012 off the
615 west coast of El Hierro (Canary Islands, Spain)" by Pérez NM, Somoza L, Hernández PA,
616 González de Vallejo L, León R, Sagiya T, Biain A, González FJ, Medialdea T, Barrancos J,
617 Ibáñez J, Sumino H, Nogami K and Romero C [Bull Volcanol (2014) 76:882-896]. *Bulletin of*
618 *Volcanology 77*: 62. doi:10.1007/s00445-015-0947-6.
619 Carapezza, M.L., Inguaggiato, S., Brusca, L., & Longo, M. (2004). Geochemical precursors of
620 the activity of an open-conduit volcano: The Stromboli 2002–2003 eruptive events.
621 *Geophysical Research Letters 31*, L07620. doi:10.1029/2004GL019614.
622 Carracedo, J.C., Rodríguez-Badiola, E. R., Guillou, H., de la Nuez, J., & Pérez-Torrado, F. J.
623 (2001). Geology and volcanology of La Palma and El Hierro, Western Canaries. *Estudios*
624 *Geológicos 57*(5-6), 175-273.
625 Cochran, E. S., Vidale, J. E., & Tanaka, S. (2004). Earth tides can trigger shallow thrust fault
626 earthquakes. *Science 306*, 1164-1166.
627 Crockett, R. G. M., Gillmore, G. K., Phillips, P. S., & Gilbertson, D. D. (2006). Tidal
628 synchronicity of the 26 December 2004 Sumatran earthquake and its aftershocks. *Geophysical*
629 *Research Letters, 33*, L19302. doi: 10.1029/2006GL027074.

630 Domínguez Cerdeña, I., del Fresno, C., & Gomis Moreno, A. (2014). Seismicity patterns prior to
631 the 2011 El Hierro Eruption. *Bulletin of the Seismological Society of America 104*, Vol 1. doi:
632 10.1785/0120130200.
633 Dzurisin, D. (1980). Influence of fortnightly earth tides at Kilauea volcano, Hawaii. *Geophysical*
634 *Research Letters 7*, 925-928.
635 Emter, D. (1997). Tidal triggering of earthquakes and volcanic events, in *Tidal Phenomena,*
636 *Lecture Notes in Earth Sciences vol. 66*, edited by H. Wilhelm, W. Zürn, and H-G. Wenzel,
637 pp. 293-309, Springer, New York, USA.
638 Fischer, T., Kalenda, P., & Skalský, L. (2006). Weak tidal correlation of NW-Bohemia/Vogtland
639 earthquake swarms. *Tectonophysics 424*, 259-269. doi: 10.1016/j.tecto.2006.03.041.
640 Fortin, M-J., & Jacquez, G. (2000). Randomization Tests and Spatially Auto-Correlated Data.
641 *Bulletin of the Ecological Society of America 81*, 201-205. doi: 10.2307/20168439.
642 García, A., Fernández-Ros, A., Berrocoso, M., Marrero, J. M., Prates, G., De la Cruz-Reyna, S.,
643 & Ortiz, R. (2014). Magma displacements under insular volcanic fields, applications to
644 eruption forecasting: El Hierro, Canary Islands, 2011-2013. *Geophysical Journal*
645 *International 197*, 322-334. doi: 10.1093/gji/ggt505.
646 García-Yeguas, A., Ibáñez, J. M., Koulakov, I., Jakovlev, A., Romero-Ruiz, M. C., & Prudencio,
647 J. (2014). Seismic tomography model reveals mantle magma sources of recent volcanic activity
648 at El Hierro Island (Canary Islands, Spain). *Geophysical Journal International 199*:1739–1750.
649 https://doi.org/10.1093/gji/ggu339.
650 Girona, T., Huber, Ch., & Caudron, C. (2018). Sensitivity to lunar cycles prior to the 2007
651 eruption of Ruapehu volcano. *Scientific Reports, 8*:1476. doi: 10.1038/s41598-018-19307-z.

González, P. J., Samsonov, S. V., Pepe, S., Tiampo, K. F., Tizzani, P., Casu, F., Fernández, J., Camacho, A. G., & Sansosti, E. (2013). Magma storage and migration associated with the 2011-2012 El Hierro eruption: Implications for crustal magmatic systems at oceanic island volcanoes. *Journal of Geophysical Research: Solid Earth, 118*, 4361-4377. doi: 10.1002/jgrb.50289.

Gorbatikov, A. V., Montesinos, F. G., Arnoso, J., Stepanova, M. Y., Benavent, M., & Tsukanov, A. A. (2013). New features in the subsurface structure model of El Hierro Island (Canaries) from low-frequency microseismic sounding: An insight into the 2011 seismo-volcanic crisis. *Surveys in Geophysics 34*(4), 463–489. doi:10.1007/s10712-013-9240-4.

Hamilton, W. L. (1973). Tidal cycles of volcanic eruptions - fortnightly to 19 yearly periods. *Journal of Geophysical Research 78*, 3363-3375.

Hartzell, St., & Heaton, T. H. (1989). The fortnightly tide and the tidal triggering of earthquakes. *Bulletin of the Seismological Society of America 79*, 1282-1286.

Heaton, T. H. (1982). Tidal triggering of earthquakes. *Bulletin of the Seismological Society of America 72*, 2181-2200.

Hough, S. (2018). Do large (Magnitude ≥8) Global earthquakes Occur on Preferred Days of the Calendar Year or Lunar Cycle? *Seismological Research Letters*. doi: 10.1785/0220170154.

Ibáñez, J. M., De Angelis, S., Díaz-Moreno, A., Hernández, P., Alguacil, G., Posadas, A., & Pérez, N. (2012). Insights into the 2011-2012 submarine eruption off the coast of El Hierro (Canary Islands, Spain) from statistical analyses of earthquake activity. *Geophysical Journal International 191*(2), 659-670.

673 Kansowa, T., & Tatnall, A. (2010). Earth tides and earthquake, in *Proceedings of 'Fringe 2009',*
674 *ESRIN, Frascali, Italy, 30 November – 4 December 2009 (ESA SP-677, March 2010), ESA*
675 *Communications*, edited by H. Lacoste-Francis, ESTEC, Noordwijk, The Netherlands.
676 Kasahara, J., Shigeru, N., & Koketsu, K. (2001). Tidal influence on the 2000 Miyake-jima
677 eruption and its implications for hydrothermal activity and volcanism. *Proceedings of the*
678 *Japan Academy, vol. 77*, 6, 98-103.
679 King, G. C. P., Stein, R. S., & Lin, J. (1994). Static stress changes and the triggering of
680 earthquakes. *Bulletin of the Seismological Society of America 84*, 935-953.
681 Klein, F. W. (1976). Earthquake swarms and the semidiurnal solid earth tides. *Geophysical*
682 *Journal of the Royal Astronomical Society 45*, 245-295.
683 Lambert, A., Kao, H., Rogers, G., & Courtier, N. (2009). Correlation of tremor activity with tidal
684 stress in the northern Cascadia subduction zone. *Journal of Geophysical Research 114*. doi:
685 10.1029/2008JB006038.
686 López, C., et al. (2012). Monitoring the volcanic unrest of El Hierro (Canary Islands) before the
687 onset of the 2011–2012 submarine eruption. *Geophysical Research Letters 39*, L13303.
688 doi:10.1029/2012GL051846.
689 Machado, F. (1967). Activity of the Atlantic Volcanoes, 1947-1965. *Bulletin of Volcanology 30*:
690 29-34. https://doi.org/10.1007/BF02597652
691 Martí, J., *et al.* (2013). Causes and mechanisms of the 2011–2012 El Hierro (Canary Islands)
692 submarine eruption. *Journal of Geophysical Research: Solid Earth 118*, 823–839. doi:
693 10.1002/jgrb.50087.

694 Masson, D., Watts, A., Gee, M., Urgeles, R., Mitchell, N., Bas, T. L., & Canals, M. (2002).
695 Slope failures on the flanks of the western Canary Islands. *Earth-Science Reviews 57*(1-2), 1-
696 35.
697 Matsumoto, K., Takanezawa, T., & Ooe, M. (2000). Ocean tide models developed by
698 assimilating TOPEX/POSEIDON altimeter data into hydrodynamical model: A global model
699 and a regional model around Japan. *Journal of Oceanography 56*, 567-581.
700 Mauk, F. J., & Johnston, M. J. S. (1973). On the triggering of volcanic eruptions by earth tides.
701 *Journal of Geophysical Research 78*, 3356-3362.
702 McNutt, S. R., & Beavan, R. J. (1981). Volcanic earthquakes at Pavlof Volcano correlated with
703 the solid earth tide. *Nature 294*, 615 – 619.
704 McNutt, S. R., & Beavan, R. J. (1984). Patterns of earthquakes and the effect of solid earth and
705 ocean load tides at the Mt. St. Helens prior to the May 18, 1980, eruption. *Journal of*
706 *Geophysical Research 89*, 3075-3086.
707 Melián, G., Hernández, P. A., Padrón, E., Pérez, N. M., Barrancos, J., Padilla, G., Dionis, S.,
708 Rodríguez, F., Calvo, D., & Nolasco, D. (2014). Spatial and temporal variations of diffuse
709 CO_2 degassing at El Hierro volcanic system: Relation to the 2011–2012 submarine eruption.
710 *Journal of Geophysical Research: Solid Earth 119*, 6976–6991. doi:10.1002/2014JB011013.
711 Métivier, L., de Viron, O., Conrad, C. P., Renault, S., Diament, M., & Patau, G. (2009).
712 Evidence of earthquake triggering by the solid earth tides. *Earth and Planetary Science*
713 *Letters 278*, 370-375. doi: 10.1016/j.epsl.2008.12.024.
714 Mignan, A., & Woessner, J. (2012). Estimating the magnitude of completeness for earthquake
715 catalogs. *Community Online Resource for Statistical Seismicity Analysis*. doi: 10.5078/corssa-
716 00180805. Available at http://www.corssa.org.

Munk, W. H., & Cartwright, D. E. (1966). Tidal Spectroscopy and Prediction. *Philosophical Transactions of the Royal Society A 259*, 533-581.

Nakata, R., Suda, N., & Tsuruoka, H. (2008). Non-volcanic tremor resulting from the combined effect of Earth tides and slow slip events. *Nature Geoscience 1*, 676–678. doi: 10.1038/ngeo288.

Noreen, E. (1989). *Computer intensive methods for testing hypothesis*. John Wiley & Sons, Ltd., New York, USA.

Pérez, N. M., Somoza, L., Hernández, P. A., González de Vallejo, L., León, R., Sagiva, T., Biain, A., González, F. J., Medialtea, T., Barrancos, J., Ibáñez, J., Sumino, H., Nogami, K., & Romero, C. (2014). Evidence from acoustic imaging for submarine volcanic activity in 2012 off the west coast of El Hierro (Canary Islands, Spain). *Bulletin of Volcanology 76*: 882. https://doi.org/10.1007/s00445-014-0882-y.

Pérez, N. M., Somoza, L., Hernández, P. A., González de Vallejo, L., León, R., Sagiva, T., Biain, A., González, F. J., Medialtea, T., Barrancos, J., Ibáñez, J., Sumino, H., Nogami, K., & Romero, C. (2015). Reply to comment from Blanco et al. (2015) on "Evidence from acoustic imaging for submarine volcanic activity in 2012 off the west coast of El Hierro (Canary Islands, Spain)" by Pérez et al. [Bull. Volcanol. (2014), 76:882–896]. *Bulletin of Volcanology 77*: 63. doi:10.1007/s00445-015-0948-5.

Press, W. H., Flannery, B. P., Teukolsky, S. A., & Vetterling, W. T. (1992). *Numerical Recipes in Fortran 77 – The Art of Scientific Computing*. Cambridge Univ. Press, New York, USA. doi: 10.2277/052143064X.

Reasenberg, P. (1985). Second-Order Moment of Central California Seismicity, 1969-1982. *Journal of Geophysical Research 90*, 5479-5495.

Royer, A. A., Thomas, A. M., & Bostock, M. G. (2015). Tidal modulation and triggering of low-frequency earthquakes in northern Cascadia. *Journal of Geophysical Research Solid Earth 120*, 384–405. doi:10.1002/2014JB011430.

Rubinstein, J. L., La Rocca, M., Vidale, J. E., Creager, K. C., & Wech, A. G. (2008). Tidal modulation of nonvolcanic tremor. *Science 319*, 186-189.

Rydelek, P. A., Davis, P. M., & Koyanagi, R. Y. (1988). Tidal triggering of earthquake swarms at Kilauea volcano, Hawaii. *Journal of Geophysical Research 93*, 4401-4411.

Sainz-Maza Aparicio, S., Arnoso Sampedro, J., Gonzalez Montesinos, F., & Martí Molist, J. (2014). Volcanic signatures in time gravity variations during the volcanic unrest on El Hierro (Canary Islands). *Journal of Geophysical Research Solid Earth 119*, 5033–5051. doi:10.1002/2013JB010795.

Satoshi, I., Yave, S., & Tanaka, Y. (2016). Earthquake potential revealed by tidal influence on earthquake size–frequency statistics. *Nature Geoscience 9*, 834-837.

Scholz, C. H., Tan, Y. J. & Albino, F. (2019). The mechanism of tidal triggering of earthquakes at mid-ocean ridges. *Nat Commun 10*, 2526. https://doi.org/10.1038/s41467-019-10605-2

Shimozuru, D. (1987). Tidal effects of Hawaiian volcanism. *US Geological Survey Professional Paper 1350*: 1337-1343.

Simpson, J. F. (1967). Earth tides as a triggering mechanism for earthquakes. *Earth and Planetary Science Letters 2*, 473-478.

Smith, S. W., & Sammis, C. G. (2002). Revisiting the tidal activation of seismicity with a Damage Mechanics and friction point of view, in *3rd ACES Workshop Proceedings*, edited by A. Donnellan and P. Mora, pp. 327-332, Mani, Hawai, USA.

762 Sottili, G., & Palladino, D. M. (2012). Tidal modulation of eruptive activity at open-vent
763 volcanoes: evidence from Stromboli, Italy. *Terra Nova 24*, 233–237. doi: 10.1111/j.1365-
764 3121.2012.01059.x.
765 Sottili, G., Martino, S., Palladino, D. M., Paciello, A., & Bozzano, F. (2007). Effects of tidal
766 stresses on volcanic activity at Mount Etna, Italy. *Geophysical Research Letters, 34*, L01311.
767 doi: 10.1029/2006GL028190.
768 Stroncik, N, Klügel, A., & Hansteen, T. (2009). The magmatic plumbing system beneath El
769 Hierro (Canary Islands): constraints from phenocrysts and naturally quenched basaltic glasses
770 in submarine rocks. *Contributions to Mineralogy and Petrology 157*, 593-607.
771 Tanaka, S. (2010). Tidal triggering of earthquakes precursory to the recent Sumatra megathrust
772 earthquakes of 26 December 2004 (Mw 9.0), 28 March 2005 (Mw 8.6), and 12 September
773 2007 (Mw 8.5). *Geophysical Research Letters 37*, L02301. doi: 10.1029/2009GL041581.
774 Tanaka, S., Ohtake, M., & Sato, H. (2002). Evidence for tidal triggering of earthquakes as
775 revealed from statistical analysis of global data. *Journal of Geophysical Research 107*, 2211.
776 doi: 10.1029/2001JB001577.
777 Thomas, A. M., Nadeau, R. M., & Bürgmann, R. (2009). Tremor-tide correlations and near-
778 lithostatic pore pressure on the deep San Andreas fault. *Nature 462*, 1048-1051. doi:
779 10.1038/nature08654.
780 Thomas, A. M., Bürgmann, R., Shelly, D. R., Beeler, N. M., & Rudolph, M. L. (2012). Tidal
781 triggering of low frequency earthquakes near Parkfield, California: Implications for fault
782 mechanics within the brittle-ductile transition. *Journal of Geophysical Research 117*, B05301.
783 doi: 10.1029/2011JB009036.

784 Tsuruoka, H., Ohtake, M., & Sato, H. (1995). Statistical test of the tidal triggering of
785 earthquakes: Contribution of the ocean tide loading effect. *Geophysical Journal International*
786 *122*, 183-194.
787 van Stiphout, T., Zhuang, J., & Marsan, D. (2012). Seismicity declustering. *Community Online*
788 *Resource for Statistical Seismicity Analysis*. doi: 10.5078/corssa-52382934. Available at
789 http://www.corssa.org.
790 Varga, P., & Grafarend, E. (1996). Distribution of the lunisolar tidal elastic stress tensor
791 components within the Earth's mantle. *Physics of the Earth and Planetary Interiors 93*, 285-
792 297.
793 Vidale, J. E., Agnew, D. C., Johnston, M. J. S., & Oppenheimer, D. H. (1998). Absence of
794 earthquake correlation with Earth tides: an indication of high preseismic fault stress rate.
795 *Journal of Geophysical Research 103*, 24567-24572.
796 Waldhauser F., & Ellsworth, W. L. (2000). A double-difference earthquake location algorithm:
797 Method and application to the northern Hayward fault. *Bulletin of the Seismological Society*
798 *of America, 90*, 1353-1368.
799 Wasserstein, R. L., & Lazar, N. A. (2016). The ASA's Statement on p-Values: Context, Process,
800 and Purpose. *The American Statistician 70*:2, 129-133. doi: 10.1080/00031305.2016.1154108.
801 Watts, A. B. (1994). Crustal structure, gravity anomalies and flexure of lithosphere in the
802 vicinity of the Canary Islands. *Geophysical Journal International 119*(2), 648-666.
803 Wilcock, W. S. D. (2009). Tidal triggering of earthquakes in the Northeast Pacific Ocean.
804 *Geophysical Journal International 179*, 1055-1070. doi: 10.1111/j.1365-246X.2009.04319.x.
805 Wonnacot, T. H., & Wonnacot, R. J. (1977). *Introductory Statistics*. Wiley, New York.

806 Xu, Y-J., Wu, X-P., Yan, C-H, Huang, Y., Wang, Y., & Li, T. (2011). The Tidal Coulomb
807 Failure Stresses on Various Kinds of Seismic Fault. *Chinese Journal of Geophysics 54*, 197–
808 206. doi: 10.1002/cjg2.1601.
809 Young, D., & Zürn, W. (1979). Tidal triggering of earthquakes in the Swabian Jura? *Journal of*
810 *Geophysics 45*, 171-182.
811

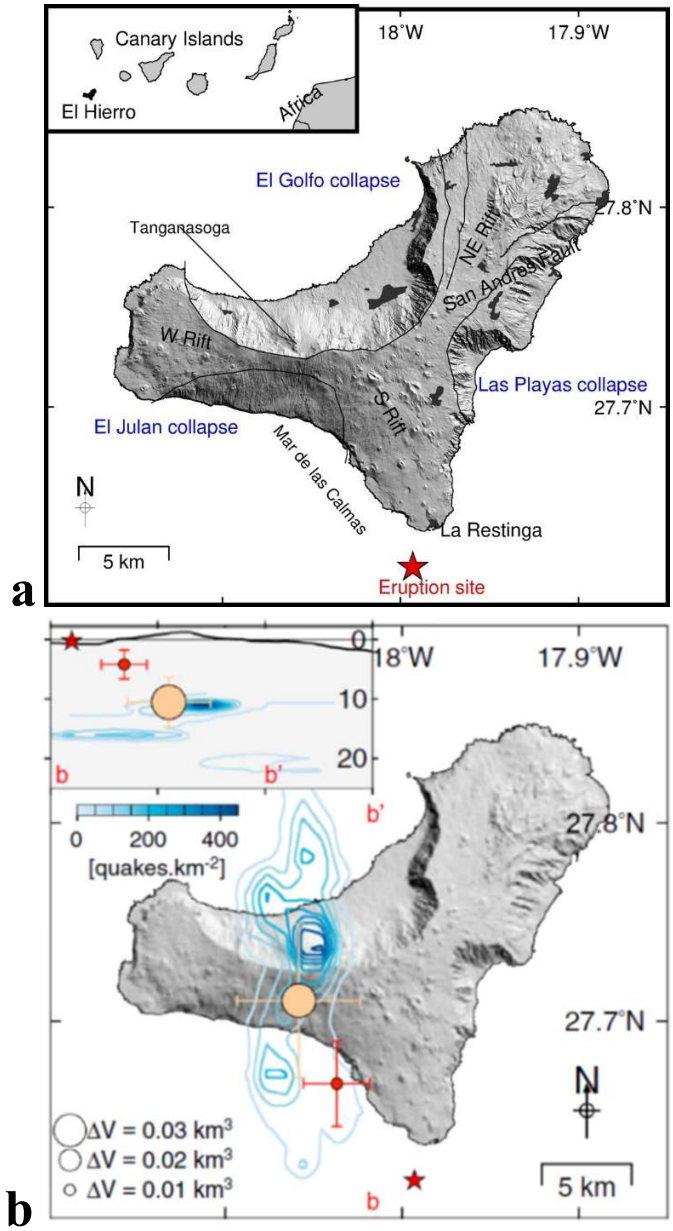

Figure 1. (a) Map of El Hierro Island and the three rift zones (Northeastern, Western-Northwestern, and South-Southeastern) showing topography (shaded topography). Flank collapses and faults are denoted with black lines. Populated areas are shown with gray polygons. Inset: El Hierro (EH) location in the Canary Islands NW of the African continent. Red star indicates the approximate location of the eruption site (same in all map figures). **(b)** Model of the magma migration process culminating in the submarine eruption in 2011 (October), with the location of the best-fitting spherical point sources: orange, deep crustal source (crust-mantle reservoir, or CMR following the notation by González et al., 2013); and dark red, the shallower crustal reservoir. Seismicity flux (events/km^2), which represents the 2-D clustering of background seismicity, is shown the background. Inset shows the vertical cross section b-b' (Modified from González et al., 2013).

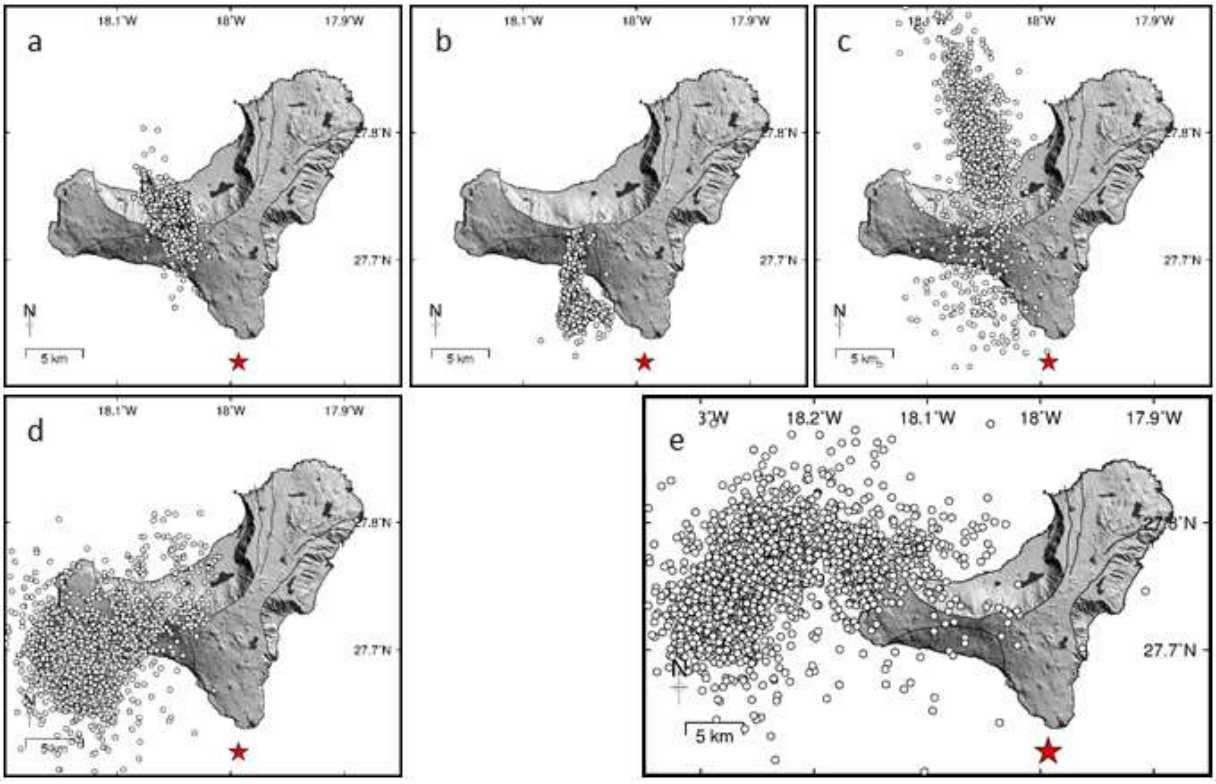

Figure 2. Location of earthquakes that occurred during the different phases detailed in the manuscript: **a**) *Phase 1*, part 1 (2011-07-17 to 2011-09-14); **b**) *Phase 1*, part 2 (2011-09-15 to 2011-10-10); **c**) *Phase 2* (2011-10-15 to 2012-03-05); **d**) Phase 3 (2012-06-14 to 2012-08-21); **e**) Phase 4 (2013-03-17 to 2013-04-30). Only events of $M \geq 1.5$ are shown.

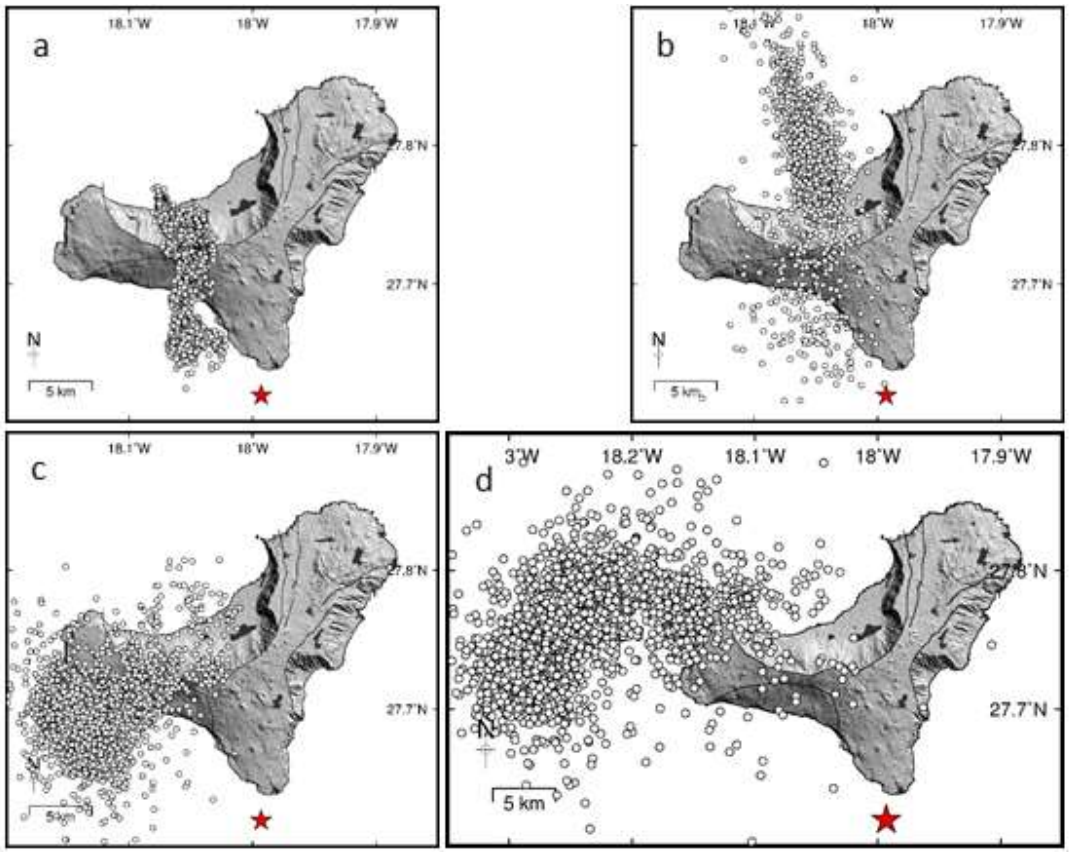

Figure 3. Location of the earthquakes in the four big clusters found in the catalog: **a**) *cluster C1*, corresponding to *Phase 1*; **b**) *cluster C2*, corresponding to *Phase 2*; **c**) *cluster C3*, corresponding to *Phase 3*; **d**) *cluster C4*, corresponding to *Phase 4*.

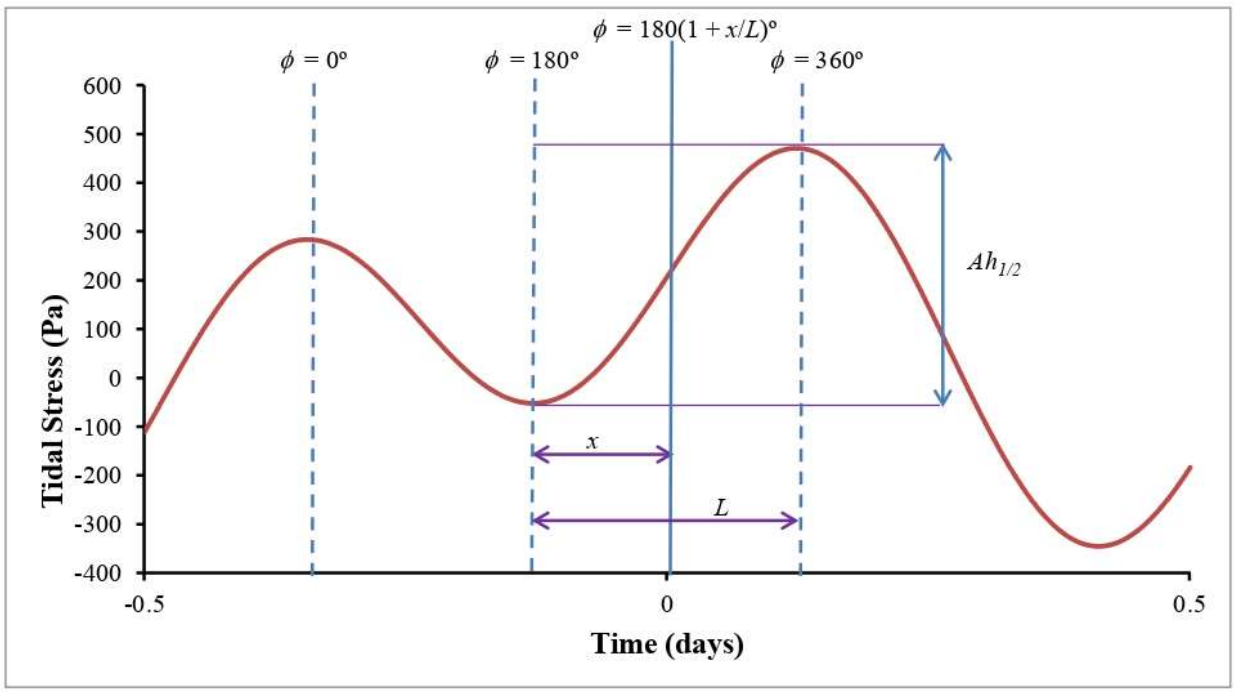

Figure 4. Schematic of the tidal phase method (Wilcock, 2009). The terms $Ah_{1/2}$ and L are the amplitude and time length of the half cycle in which the event occurs, respectively. x is the time difference between the occurrence time of the earthquake and phase $\phi = 180^{o}$, positive when the event occurs after phase $\phi = 180^{o}$ and negative when it happens prior to phase $\phi = 180^{o}$.

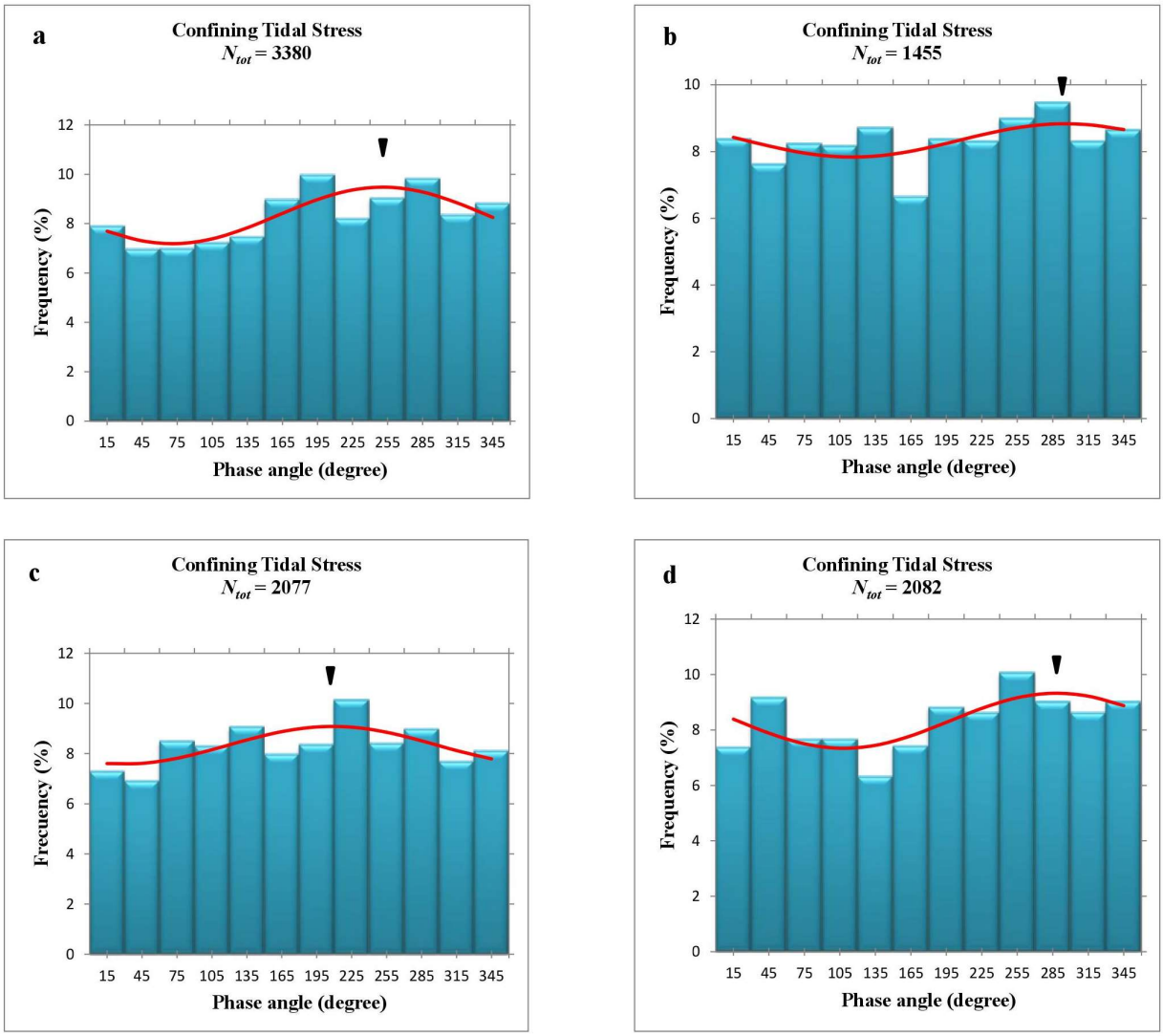

Figure 5. Histograms of the frequency distribution of tidal phase angles for all events in *clusters*: (**a**) *C1* (period 2011-07-21 / 2011-10-10); (**b**) *C2* (2011-10-17 to 2012-01-01); (**c**) *C3* (2012-06-25 to 2012-08-13); (**d**) *C4* (2013-03-18 to 2013-04-28). N_{tot} is the number of events of each subset. The curve represents a sinusoidal function fitted to the frequency distribution. The peak of the fitted curve is indicated by a triangle.

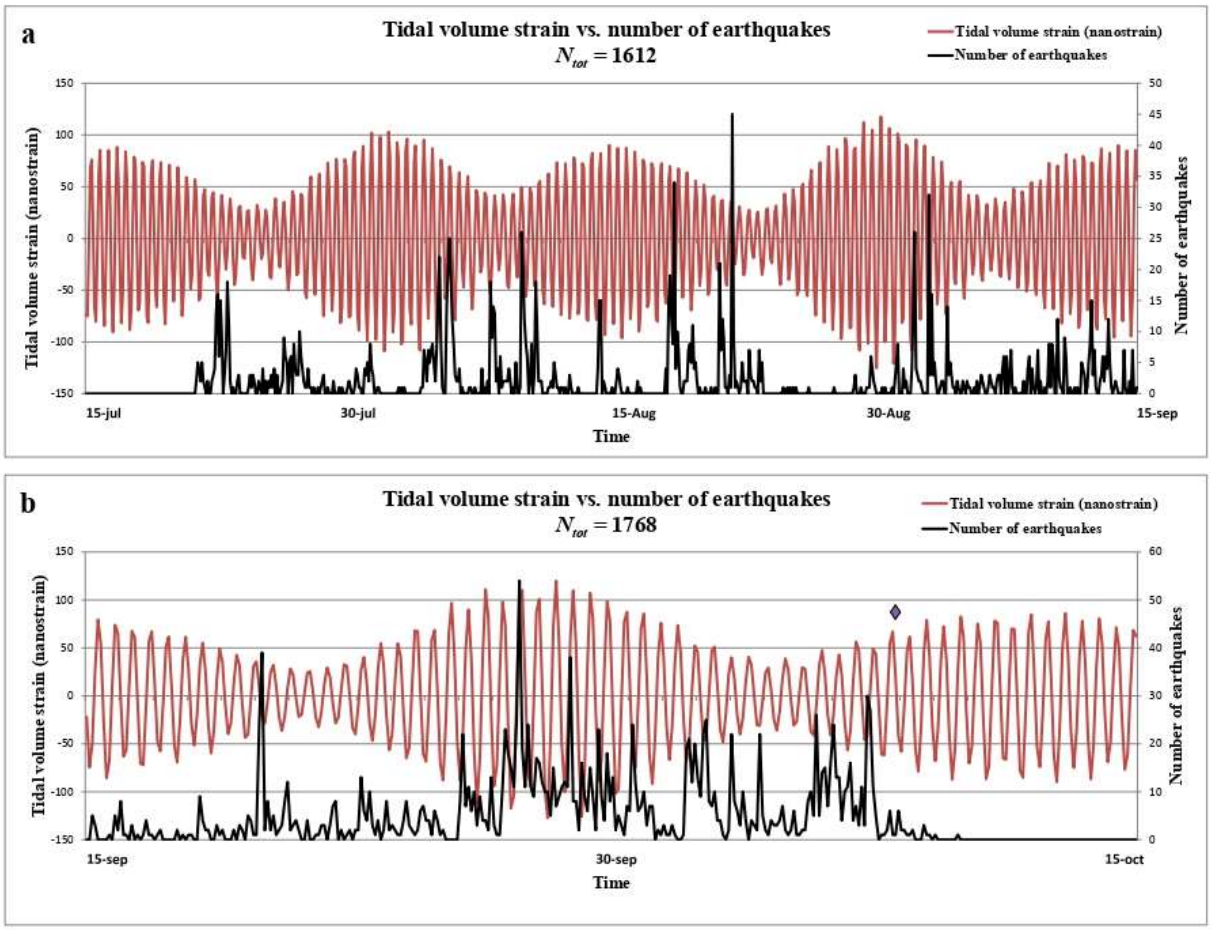

Figure 6. Red line shows tidal volume strain in the setting of the shallow reservoir (see text for details) during a period covering all the seismic activity prior to the submarine eruption (Phase1). Black line represents the number of earthquakes recorded in *cluster C1* every two hours alongside the same time period. The plot has been divided in two parts: (**a**) 2011-07-15 to 2011-09-14; (**b**) 2011-09-15 to 2011-10-15. N_{tot} is the number of earthquakes represented in each part. The purple diamond in (**b**) marks the occurrence of the M = 4.3 earthquake (2011 October 8) which is considered as the event opening a path for the final episode of magma rising towards the surface two days later (González et al., 2013).

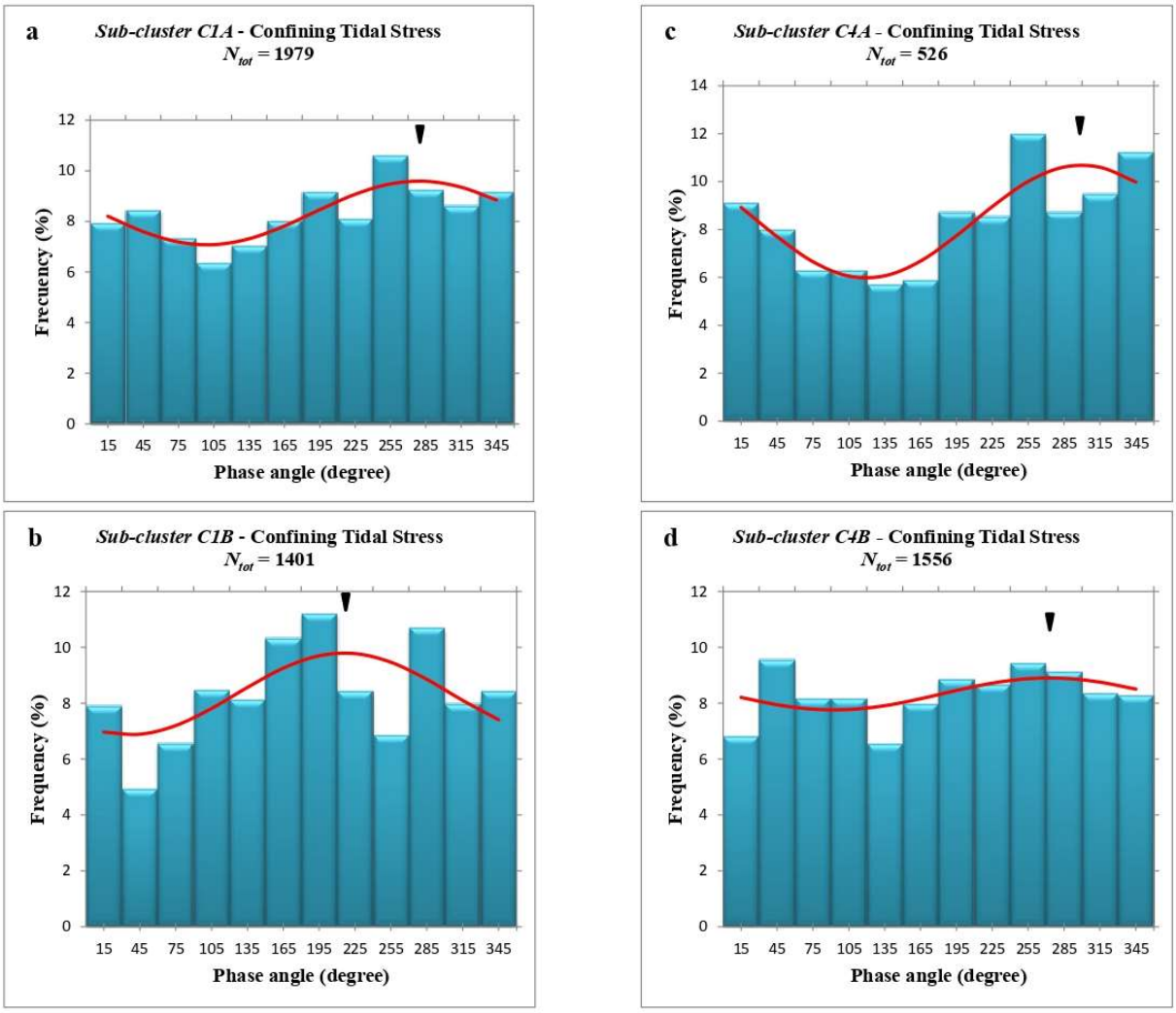

Figure 7. Histograms of the frequency distribution of tidal phase angles for tidal confining stress: (**a**) for *sub-cluster C1A* (2011-07-17 to 2011-09-25); (**b**) for *sub-cluster C1B* (2011-09-26 to 2011-10-10). Histograms of the frequency distribution of tidal confining stress phase angles for all events for *cluster C4* according to depth: (**c**) *sub-cluster C4A*, earthquakes with hypocenters in the depth range between 0 and 15 km; (**d**) *sub-cluster C4B*, earthquakes with depth greater than 15 km. N_{tot} is the number of events of each subset. The curve represents a sinusoidal function fitted to the frequency distribution. The peak of the fitted curve is indicated by a triangle.

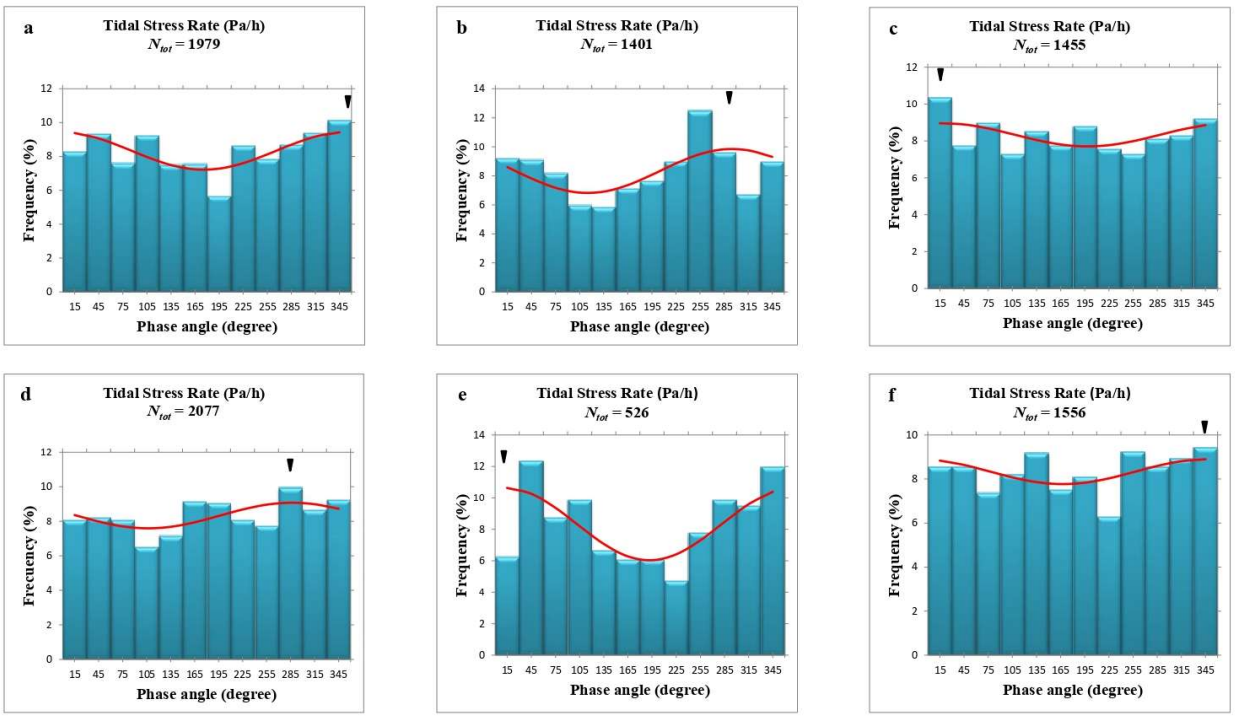

Figure 8. Histograms of the frequency distribution of tidal confining stress rates for all events in *clusters* and *sub-clusters*: (**a**) *C1A* (2011-07-17 to 2011-09-25); (**b**) *C1B* (2011-09-26 to 2011-10-10); (**c**) *C2* (2011-10-17 to 2012-01-01); (**d**) *C3* (2012-06-25 to 2012-08-13); (**e**) *C4A* (2013-03-18 to 2013-04-28, events with depth ≤ 15 km only); (**f**) *C4B* (2013-03-18 to 2013-04-28, events with depth > 15 km only). N_{tot} is the number of events of each subset. The curve represents a sinusoidal function fitted to the frequency distribution. The peak of the fitted curve is indicated by a triangle.

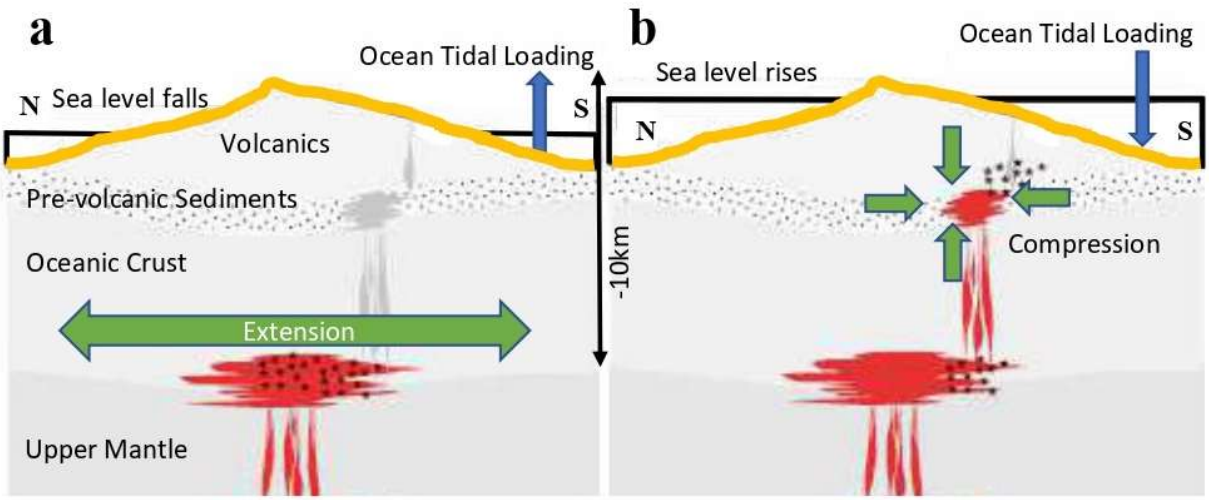

Figure 9. Schematics of the proposed sequence of volcano activity resulting in the observed correlations between tidal confining stress and earthquakes. (**a**) Time period 2011-07-17 to 2011-09-25. Magma begins to accumulate in the deep CMR, and then moves longitudinally around the center of the CMR. With low tide, sea level falls and the weight of the ocean over the seafloor of the island diminishes, which means compression decreases and extension increases. High values of extensional tidal confining stress rates may favor the magma displacements and encourage extensional faulting and the seismic activity related to this time period may be related to higher values of tidal stress rates. (**b**) Time period 2011-09-26 to 2011-10-10. Magma ascends towards a shallow reservoir smaller than the deep CMR and accumulates there until the eruption began on October 10, 2011. With magma concentrated in a reduced volume, magmatic activity in the shallow reservoir may be more sensitive to small changes in tidal stress compression. When the tides are high, sea level rises and the compression exerted on the seafloor by the body of water increases, promoting both magma ascent and the build-up of pressure within the magma chamber. Tidal confining stress compression, together with tectonic and volcanic stresses, would squeeze the magma chamber, escaping through zones of weakness to ascend and favoring seismic activity. (Modified from González et al., 2013)

Cluster	Time period	Number of events	P_s value	$\overline{B}$
C1	2011-07-21 / 2011-10-10	3380	**0.3999e-06**	**62435.7879**
C2	2011-10-17 / 2012-01-01	1455	0.1475	1.3033
C3	2012-06-25 / 2012-08-13	2077	**0.0112**	7.2973
C4	2013-03-18 / 2013-04-28	2082	**0.0008**	**63.1326**

Table 1. Results of the application of Schuster's test and calculation of the upper bound $\overline{B}$ of the Bayes factor B to the earthquake *clusters C1-C4*. P_s is the probability that the phase angle distribution to be random, according to Schuster's test. $\overline{B}$ is derived from P_s according to expression (5). Occurrences where $P_s < 0.05$ or $\overline{B} > 16$ are in bold. Type of tidal stress considered is confining.

988

989
990

Cluster	Number of events	P_s value	Segment length: 5º		Segment length: 2.5º	
			NSIG ($P^* \leq P_s$) for 10000 permutations	SL MC_{sl}	NSIG ($P^* \leq P_s$) for 10000 permutations	SL MC_{sl}
C1	3380	**0.3999e-06**	1	**0.0002**	**0**	**0.0001**
C2	1455	0.1475	1767	0.1768	1911	0.1912
C3	2077	**0.0112**	279	**0.0280**	140	**0.0141**
C4	2082	**0.0008**	22	**0.0023**	13	**0.0014**

991

992 **Table 2**. Results of the application of Schuster's test and a Monte Carlo permutation test (10000
993 simulations) to the earthquake *clusters C1-C4*. Different segment lengths were applied[a]. P_s is the
994 probability that the phase angle distribution in the original catalog to be random, according to
995 Schuster's test. For each permutation, a Schuster probability value P^* is obtained. NSIG is the
996 number of permutations where $P^* \leq P_s$ for each cluster. SL means "significance level". The
997 significance level MC_{sl} of the permutation test is obtained according to expression (3) in section
998 3.3. Occurrences where $P_s < 0.05$ or $MC_{sl} < 0.05$ are in bold.

999

Cluster	$N_{i,obs}$	$N_{i,obs}/N_{tot}$	P_i	$\overline{B}$
C1	1835	0.5429	**0.33e-06**	**74696.6798**
C2	759	0.5216	0.0520	2.3923
C3	1076	0.5181	0.0522	2.3865
C4	1129	0.5423	**0.62e-04**	**612.4390**

Table 3. Results of the binomial test for the confining tidal stress in the seismic crisis of El Hierro. N_{tot} is the number of events of each subset. $N_{i,obs}$ is the number of events observed in the increasing-tide phase angle half cycle ($180^o < \phi \leq 360^o$). P_i is the probability of getting a number of increasing-tide phase angle events greater or equal to the observed number $N_{i,obs}$, assuming the null hypothesis that earthquakes are not influenced by tidal stress. $\overline{B}$ is derived from P_i according to expression (5). Occurrences where $P_i < 0.05$ or $\overline{B} > 16$ are in bold.

Cluster	Time period	No. of events	P_s value	$\overline{B}$	Segment length 5º		Segment length 2.5º	
					NSIG ($P^* \leq P_s$) for 10000 permutations	SL MC_{sl}	NSIG ($P^* \leq P_s$) for 10000 permutations	SL MC_{sl}
C1A	2011-07-17/ 2011-09-25	1979	**0.6514e-04**	**585.9**	35	**0.0036**	4	**0.0005**
C1B	2011-09-26/ 2011-10-10	1401	**0.1633e-04**	**2043.8**	8	**0.0009**	0	**0.0001**

Table 4. Results of the application of the statistical tests described in the text to the earthquake *clusters C1A* and *C1B*. P_s is the probability that the phase angle distribution to be random, according to Schuster's test. $\overline{B}$ is derived from P_s according to expression (5). For each permutation, a Schuster probability value P^* is obtained. NSIG is the number of permutations where $P^* \leq P_s$ for each cluster. SL means "significance level". The significance level MC_{sl} of the permutation test is obtained according to expression (3) in section 3.3. Occurrences where $P_s < 0.05$, $\overline{B} > 16$ or $MC_{sl} < 0.05$ are in bold. Type of tidal stress considered is confining.

Cluster	Time period	Number of events	P_s value	$\overline{B}$	Segment length 5º		Segment length 2.5º	
					NSIG ($P^* \leq P_s$) for 10000 permutations	SL MC_{sl}	NSIG ($P^* \leq P_s$) for 10000 permutations	SL MC_{sl}
C4A	2013-03-18 / 2013-04-28	526	**0.6458e-04**	**590.4**	7	**0.0008**	2	**0.0003**
C4B	2013-03-18 / 2013-04-28	1556	0.1578	1.2	2054	0.2055	1629	0.1630

Table 5. Results of the application of the statistical tests described in the text to the earthquake *clusters C4A* and *C4B*. *Ps* is the probability that the phase angle distribution to be random, according to Schuster's test. $\overline{B}$ is derived from P_s according to expression (5). For each permutation, a Schuster probability value P^* is obtained. NSIG is the number of permutations where $P^* \leq P_s$ for each cluster. SL means "significance level". The significance level MC_{sl} of the permutation test is obtained according to expression (3) in section 3.3. Occurrences where $P_s < 0.05$, $\overline{B} > 16$ or $MC_{sl} < 0.05$ are in bold. The type of tidal stress considered is confining.

Cluster	No. events	P_s value	$\overline{B}$	Segment length 5º		Segment length 2.5º	
				NSIG ($P^* \leq P_s$) for 10000 permutations	SL MC_{sl}	NSIG ($P^* \leq P_s$) for 10000 permutations	SL MC_{sl}
C1A	1979	**0.3395e-04**	**1052.9**	15	**0.0016**	1	**0.0002**
C1B	1401	**0.1394e-04**	**2360.3**	8	**0.0009**	3	**0.0004**
C2	1455	0.1226	1.4	2103	0.2104	1714	0.1715
C3	2077	**0.0132**	6.4	454	**0.0455**	289	**0.0290**
C4A	526	**0.4524e-04**	**812.8**	12	**0.0013**	1	**0.0002**
C4B	1556	0.1220	1.4	1771	0.1772	1319	0.1320

Table 6. Results of the application of the statistical tests described in the text considering tidal stress rates (Pa/h). P_s is the probability that the phase angle distribution to be random, according to Schuster's test. $\overline{B}$ is derived from P_s according to expression (5). For each permutation, a Schuster probability value P^* is obtained. NSIG is the number of permutations where $P^* \leq P_s$ for each cluster. SL means "significance level". The significance level MC_{sl} of the permutation test is obtained according to expression (3) in section 3.3. Occurrences where $P_s < 0.05$, $\overline{B} > 16$ or $MC_{sl} < 0.05$ are in bold. The type of tidal stress considered is confining.